

Article

Historical aerial surveys map long-term changes of forest cover and structure in the central Congo Basin

Koen Hufkens^{1,2,*} , Thalès de Haulleville³, Elizabeth Kearsley¹, Kim Jacobsen^{1,3}, Hans Beeckman³, Piet Stoffelen⁴, Filip Vandelook⁴, Sofie Meeus⁴, Michael Amara⁵, Leen Van Hirtum⁵, Jan Van den Bulcke¹, Hans Verbeeck¹, Lisa Wingate²

¹ Ghent University, Ghent, Belgium;

² INRA, UMR ISPA, Villeneuve d'Ornon, France;

³ Royal Museum for Central Africa, Tervuren, Belgium;

⁴ Botanic Garden Meise, Meise, Belgium;

⁵ National Archives of Belgium, Brussels, Belgium;

* Correspondence: koen.hufkens@gmail.com

Academic Editor: name

Version December 31, 2019 submitted to Remote Sens.

1 Abstract: Land Use and Land Cover change (LULCC) of African rainforest contribute to global carbon
2 emissions. Yet, most historical estimates of LULCC and their carbon emissions rely on non-spatially
3 explicity data in the pre-satellite era (< 1972). Past studies have expanded this pre-satellite time
4 frame with declassified satellite surveillance data or aerial surveys, but none cover the Congo Basin.
5 Here, we use historical aerial survey photos to map the extent and structure of LULCC around
6 Yangambi, central Congo Basin, in 1958. Our study leveraged Structure-from-Motion to generate
7 a large orthomosaic covering 828 km², counting 733 million pixels, at a sub meter resolution and
8 geo-referenced to ~4.7 ± 4.3 m. Primary forest in the orthomosaic was classified with a Convolutional
9 Neural Network Deep Learning approach. We used these data to quantify LULCC, landscape
10 and canopy complexity and scale above ground biomass between historical and contemporary
11 condition. We show a shift from historical highly structured industrial deforestation in 1958 (162
12 km²), to contemporary smallholder farming clearing (88 km²), increasing landscape fragmentation
13 and forest edges. Efforts to quantify canopy texture and their link to carbon storage had limited to
14 no success. Our analysis provides an insight in key spatial and temporal patterns of deforestation
15 and reforestation at a multi-decadal scale and provide a historical context to land-cover and land-use
16 change spatial patterns for past and ongoing field research in the area.

17 Keywords: Aerial survey, data recovery, CNN, Deep Learning, SfM, Congo Basin

18 1. Introduction

19 The functioning of a tropical forest, and its capacity to sequester carbon, is heavily influenced
20 by anthropogenic disturbances such as selective logging, clear felling, or slash and burn practices, all
21 increasing forest fragmentation. This increased pace in the loss of rainforest cover [1] is predicted to
22 negatively impact the function of these tropical forests, and their future capacity to sequester carbon,
23 as anthropogenic disturbances such as selective logging, clear felling, or slash and burn practices
24 collectively contribute to increasing forest fragmentation.

25 These forest fragments and their edges contain fewer large trees [2], in part due to their hotter and
26 brighter microclimates [3]. Similarly, species composition and biodiversity [4] are negatively affected.
27 Spatial disturbances also have an explicit temporal component, where the time since disturbance
28 affects the strength of the effects [5]. Deforestation and gap formation also influence the overall canopy
29 structure, where pioneer species grow taller and with narrower crowns [4,6] affecting the forest light
30 regime and carbon dynamics [7]. As such, anthropogenic factors through land-use and land cover
31 change (LULCC) heavily affect forest structure and functioning [5,8,9]. In the tropics the majority of
32 emissions originate from deforestation and forest degradation [10–12] contributing to 10–15% of the
33 total global emissions [13] and concomitant losses in biodiversity losses [14,15] and how LULCC is
34 evolving over time. Although the African rainforest is the second largest on Earth and covers ~630
35 million ha, representing up to 66 Pg of carbon storage [16], and currently loses forest at an increasing
36 pace [1]. Yet, the tropics is now becoming a large source of CO₂ to the atmosphere as deforestation and
37 forest degradation [10–12] contribute up to 10–15% of the total global CO₂ emissions [13]. Furthermore,
38 recent estimates show that 31% of recent carbon emissions are caused by edge effects alone [9]. In
39 this context, there are very few long term forest inventory plots that presently exist in the central
40 Congo Basin [17,18]. This further limits the accuracy of current biomass estimates and challenges
41 our understanding of how forest structure and function changes in the short and long term in these
42 ecosystems [19,20].

43 Historical estimates of LULCC, and their carbon emissions, exist [11,21–23], however they
44 generally rely on non-spatially explicit data in the pre-satellite era (< 1972) [24]. These analysis
45 often use FAO statistics, historical land-use sources, and/or population and socio-economic data [11],
46 as limited earlier spatial data sources are available [10,25]. For example, the Houghton [24] long-term
47 study used FAO and national censuses alongside a bookkeeping model to estimate carbon emissions
48 from LULCC. Other studies use remote sensing data, but are limited in time to recent decades [11,22].
49 These proxy based studies have a limited view on long-term direct and indirect spatial effects of
50 deforestation. As such, both the spatial structure and the fragmentation pattern of a forest combined

51 with its life history has a profound effect on carbon emssions. However, in this context remote
52 sensing assessments provide more accurate spatial information to help estimate carbon emissions [26].

53 Past studies expanded knowledge during the pre-satellite time frame through the use of now
54 declassified satellite surveillance data to map deforestation in the US, central Brazil, and post world war
55 II Germany [27,28]. In some cases these records could extend back in time even further using historical
56 aerial survey images. In northern Europe especially these data are well known and used, for example
57 to map the extent of forest cover across ~100 km² regularly, and at times using automated workflows
58 [29]. Survey data across the African continent is less common or inaccessible or both. Some studies
59 do exist, both Buitenwerf *et al.* [30] and Okeke and Karniel [31] used aerial survey images to map
60 vegetation changes in South African savannas and the Adulam Nature Reserve, respectively. Whilst
61 Frankl *et al.* [32] used 20 aerial survey images to map the Ethiopian highlands of 1935. High resolution
62 aerial or surveillance satellite images provide scientists tools to monitor forest extent and structure over
63 long time frames. Moreover, canopy texture from aerial survey images has been successfully linked
64 to above ground biomass [33–35]. Thus using texture based metrics obtained from (high resolution)
65 remote sensing data opens up possibilities to link historical aerial footage to carbon density across
66 large spatial extents [34].

67 Given the impact of LULCC on the structure and functioning of tropical forests, and their influence
68 on both carbon dynamics [19] and biodiversity [15], accurate long term reporting of historical forest
69 cover in the pre-satellite era is an imperative [36]. In this study we use a combination of historical
70 aerial photography and contemporary remote sensing data to map long-term changes in the extent
71 and structure of the tropical forest surrounding Yangambi, in the central Congo Basin at the beginning
72 of 1958 and the start of the antrophocene [37]. Our analysis provides a historical insight into important
73 LULCC spatial patterns in Yangambi, such as fragmentation and edge complexity. Our analysis further
74 contextualises the influence of changes in the forest's life history on past and current research into
75 Above Ground Carbon (AGC) storage [19] and biodiversity [15] in the central Congo Basin.

76 2. Methods

77 2.1. Historical data acquisition

78 Data for the central Congo Basin region, surrounding Kisangani, were collected in several flights
79 during the dry season of 1958 and 1959 (from 8/01/1958 to 20/02/1958 and from 28/12/1958 to
80 9/01/1959 respectively, see Appendix Figure 1) to generate topographic maps of the area, supervised
81 by the “Institut Géographique du Congo Belge” in Kinshasa (then Léopoldville). Black-and-White
82 infrared images (0.4 - 0.9 μm) were gathered along flight paths running mostly from west to east,
83 between 9 - 11h local time. Along a flight path continuous images were taken using a Wild Heerburgg

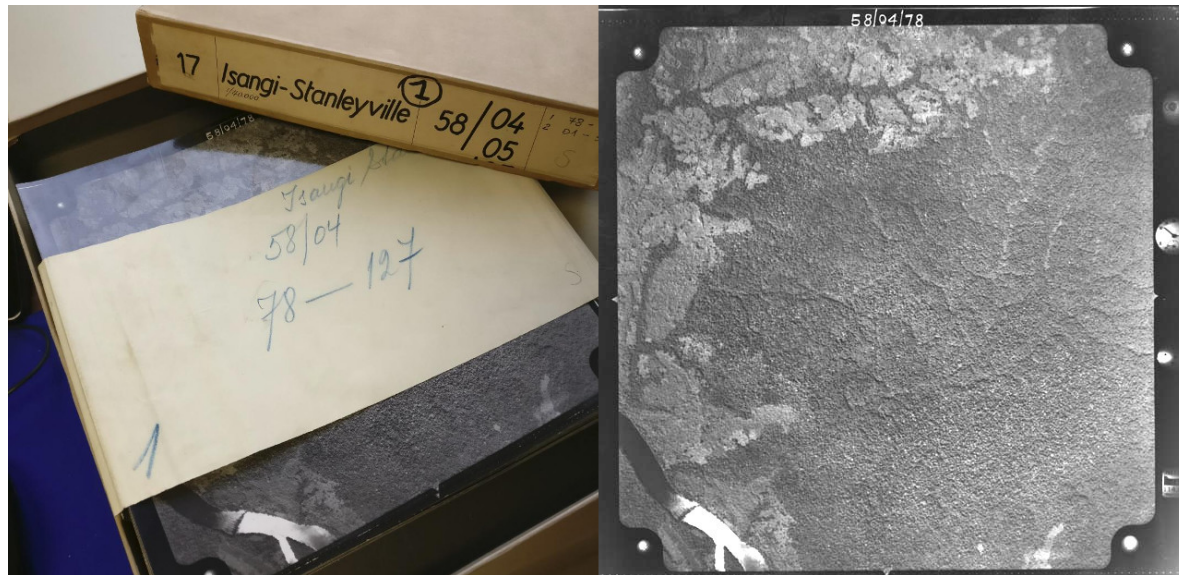


Figure 1. A box of historical aerial photographs (left) and a single aerial photograph (right) showing part of the Congo river. Note the meta-data provided in the margins of the image such as acquisition time and flight height and the solar glare on the Congo river.

84 RC5a (currently Leica Geosystems) with an Aviogon lens assembly (114.83mm / f 5.6, with a 90° view
 85 angle) resulting in square photo negative of 180 by 180 mm. Flights were flown at an average absolute
 86 altitude of ~5200 m above sea level, covering roughly 18 530 km² at an approximate scale of 1/40
 87 000. The use of the integrated autograph system ensured timely acquisition of pictures with a precise
 88 overlap (~1/3) between images. This large overlap between images together with flight parameters
 89 would allow post-processing, using stereographs, to create accurate topographic maps. Original data
 90 from this campaign are stored in the [Royal Museum for Central Africa](#) in Tervuren, Belgium (Figure 1).

91 2.2. Site selection

92 We prioritised flight paths and images that contained current day permanent sampling plots,
 93 larger protected areas, and past agricultural and forest research facilities (Figure 2). This selection
 94 provides a comprehensive mapping of the Yangambi area and the life history of the forest surrounding
 95 it. Thereafter, we selected flight paths 1 through 11 for digitization. From this larger dataset of 334
 96 images we selected 74 survey images for orthomosaic compositing and further analysis. All the
 97 selected images stem from the flight campaign made during January and February of 1958. The area
 98 includes the Yangambi village, 20 contemporary permanent sampling plots [19], past and present
 99 agricultural experimental plots [38] and large sections of the Yangambi **UNESCO Man and Biosphere**
 100 **reserve** surrounding to the west and east of the village. Although not formally mosaicked we provided
 101 a full dataset of pre-processed images using the cropping and normalization routines described below.
 102 The latter data was not used in subsequent LULCC analysis, but has been archived and made available
 103 to the public separately (see code & data availability statement below).

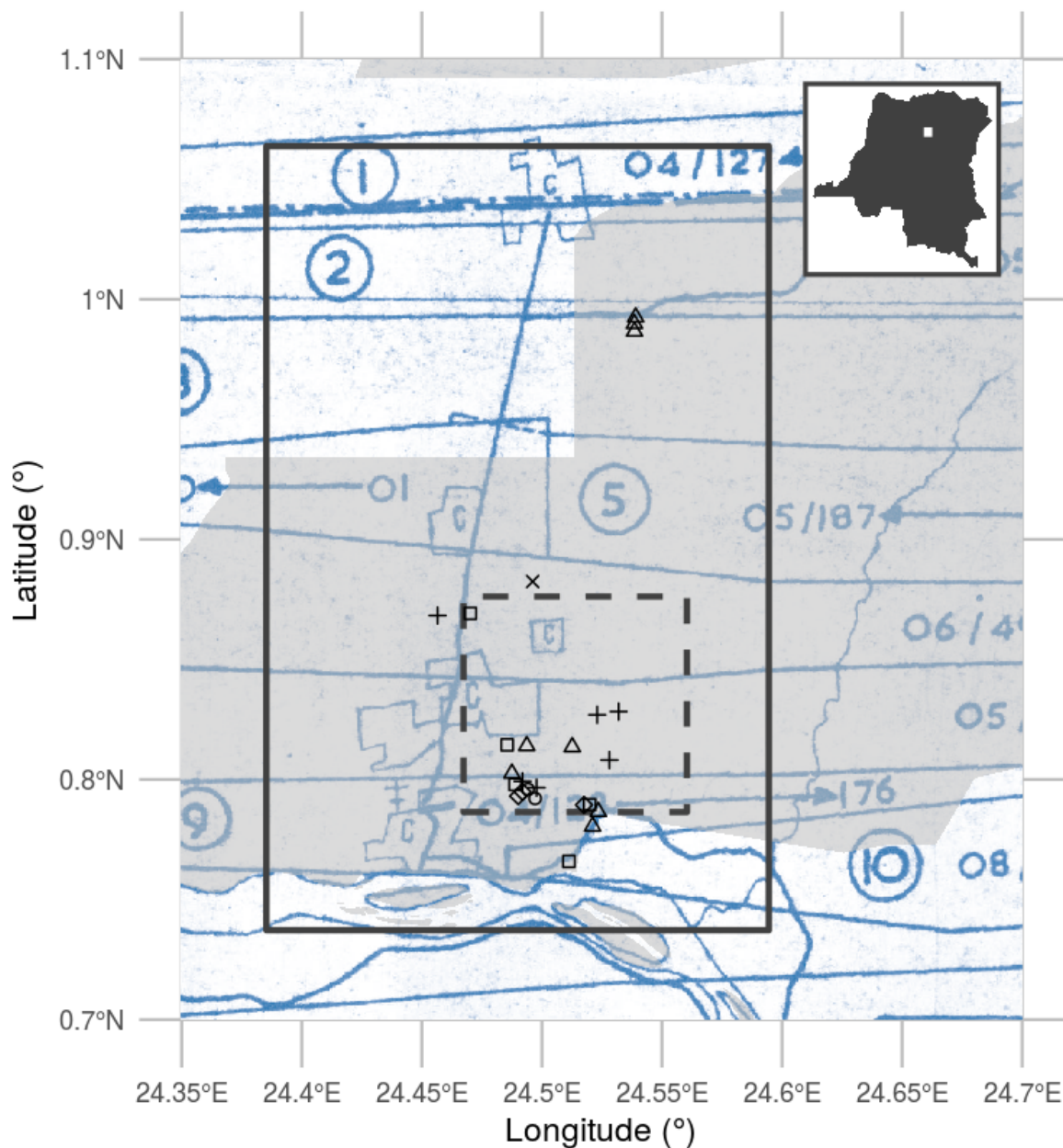


Figure 2. Overview of the historical flight paths during aerial photo acquisition and ancillary data used in this study. The bounding box of the orthomosaic data presented in this study is shown as a rectangle (23x36 km). The outline of a recent high-resolution Geo-eye panchromatic image is shown as a dashed dark grey rectangle (10x10km). The location of various permanent sampling plots are shown as x, +, and open squares and triangles for the mixed, mono-dominant and edge plots respectively. The grey polygon delineates the current day Yangambi Man and Biosphere reserve. The inset, top right, situates the greater Yangambi region with the DR Congo. The full flight plan and details are shown in Appendix Figure 1 and 2

104 2.3. *Digitization and data processing*

105 All selected images, covering the Yangambi area, were contact prints as original negatives of the
106 prints were not available. Images were scanned at a resolution exceeding their original resolution
107 (or grain) at the maximal physical resolution of an Epson A3 flatbed scanner (i.e. 2400 dpi or 160MP
108 per image) and saved as lossless tiff images. Data were normalized using contrast limited histogram
109 equalization [39] with a window size of 32 and a clip limit of 1.5. Fiduciary marks were used to rectify
110 and downsample the images into square 7700x7700 pixel images (~1200 dpi, 81MP). This resulted in a
111 dataset with digital images at a resolution that remained above the visible grain of the photographs,
112 whilst the reduced image size facilitated easier file handling and processing speed.

113 Data was processed into a georeferenced orthomosaic using a Structure from motion (SfM, Ullman
114 [40]) approach implemented in [Agisoft Metashape](#) version 1.5.2 (Agisoft LLC, St. Petersburg, Russia).
115 An orthomosaic corrects remote sensing data to represent a perfectly downward looking image, free
116 from perspective distortions due to topography and camera tilt. Using the SfM technique features,
117 areas in images with a large degree of similarity, are matched across various images to reconstruct
118 a three dimensional scene (topography) from two-dimensional image sequences. During the SfM
119 analysis we masked clouds, glare or large water bodies such as the Congo river.

120 We calculated the orthomosaic using a low resolution point cloud and digital elevation map
121 (DEM). Additional ground control points were provided to assist in the referencing of image and
122 constrain the optimization routine used in the SfM algorithm. Ground control points consisted of
123 rooftop edges of permanent structures which could be verified in both old and new aerial imagery
124 (i.e. ESRI World Imagery). Although clouds were removed during the SfM routine we did not mask all
125 clouds in the final orthomosaic to maximize forest coverage. The final scene was cropped, to provide
126 consistent wall to wall coverage of the reconstructed scene. The orthomosaic was exported as a geotiff
127 for further georeferencing in QGIS [41] using the georeferencer plugin (version 3.1.9) and additional
128 ESRI World Imagery high resolution reference data. We used 3rd degree polynomial and 16 ground
129 control points to correct the final image. Ground control points, raw image data and final processed
130 image are provided in addition to measures of uncertainty such as mean root mean squared (RMSE),
131 mean and median error across all ground control points. All subsequent analysis are executed on the
132 final geo-referenced orthomosaic or subsets of it.

133 2.4. Land-Use and Land-Cover Change

134 2.4.1. Classifying forest cover

135 We automatically delineated all natural forest in the historical data, thus excluding tree plantations,
136 thinned or deteriorated forest stands, fields and buildings. We used the Unet Convolutional Neural
137 Net (CNN, Ronneberger *et al.* [42]) architecture implemented in Keras [43] with an efficientnetb3
138 pre-processing backbone [44] running on TensorFlow [45] to train a binary classifier (i.e. forest or
139 non-forested). This methodology is increasingly being used to automate pixel-level classification in
140 (color) digital photography data [46]. Training data were collected from the orthomosaic by randomly
141 selecting 513 pixel square tiles from homogeneous forested or non-forested areas within the historical
142 orthomosaic. Homogeneous tiles were combined in synthetic landscapes using a random gaussian
143 field based binary mask (Figure 3). We generated 5000 synthetic landscapes for training, while 500
144 landscapes were generated for both the validation and the testing dataset. Source tiles did not repeat
145 across datasets to limit overfitting. In order to limit stitch line misclassifications, along the seams of
146 mosaicked images, we created synthetic landscapes with different forest tiles to mimick forest texture
147 transitions. We applied this technique to 10% of the generated synthetic landscapes. The CNN model
148 was trained for 100 epochs with a batch size of 30 using Adam optimization [47], maximizing the
149 Intersect-over-Union (IoU) using Sørensen–Dice and categorical cross-entropy loss functions. Data
150 augmentation included random cropping to 320 pixel squares, random orientation, scaling, perspective,
151 contrast and brightness shifts and image blurring. During final model evaluation we report the IoU of
152 our out-of-sample test datasets. The optimized model was used to classify the complete orthomosaic
153 using a moving window approach with a step size of 110 pixels and a majority vote across overlapping
154 areas to limit segmentation edge effects. We refer to Figure 4 for a synoptic overview of the full
155 deep learning learning workflow. In addition, we used the first acquisition of a recent pan-chromatic
156 Geo-Eye 1 stereo pair (GeoEye, 2012, Thornton, Colorado, U.S.A., order 737537, 2011-11-11 8:55h GMT
157 or 9:55h local time) to classify and visually assess the robustness of the algorithm on contemporary
158 remote sensing imagery with the same moving window approach.

159 To map long term land-use and land-cover change in the Yangambi region we used the
160 contemporary Global Forest Change version 1.6 data (GFC, tile 10N-020E) [10]. Using this data
161 we calculated the latest state of the forest with respect to the conditions at the start of 1958, 60 years
162 earlier. In our analysis we only included forested pixels which recorded no loss throughout the whole
163 2000 - 2018 period. As the resolution of the historical forest classification exceeds that of the GFC map
164 we downsampled our historical forest cover data to 30m GFC resolution. We masked out all water
165 bodies using the Global Forest Change survey data mask layer, and limited the analysis to the right

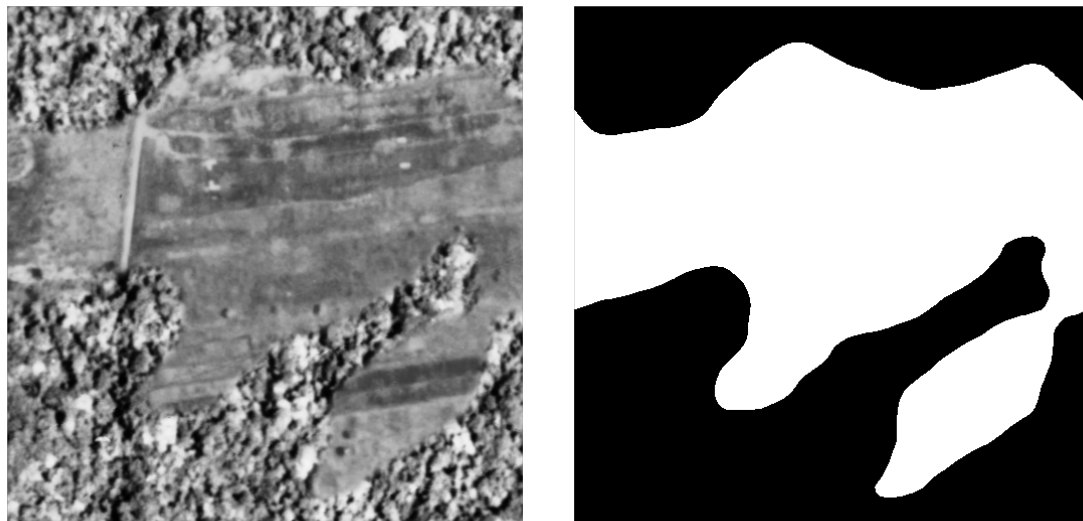


Figure 3. An example synthetic landscape, combining homogeneous forest and non-forest images into a patchy landscape using random gaussian field based masks. The left panel shows a combined synthetic landscape, while the right panel shows the corresponding forest (black) and non-forest (white) labels.

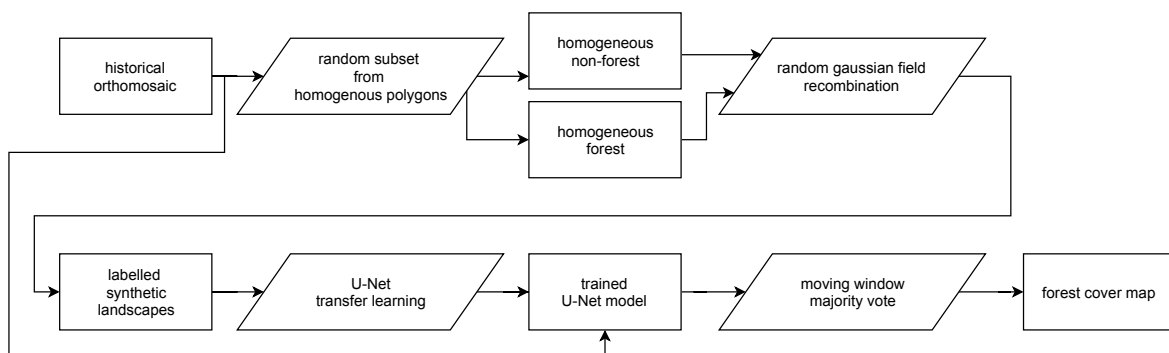


Figure 4. A diagram of the deep learning workflow followed in training a binary forest / non-forest cover convolutional neural net U-Net model to generate our forest cover map.

166 bank of the Congo river. Where the datasets overlap we provide summary statistics of deforestation,
167 reforestation and afforestation. The same methodology was used to quantify CNN model performance
168 across the Geo-Eye 1 scene.

169 **2.4.2. Landscape fragmentation & Above Ground Carbon estimates**

170 To quantify changes in the structure of forest cover and its disturbances we used spatial pattern
171 analysis landscape fragmentation metrics [48]. We report the ratio of edge to area and the fractal
172 index to quantify landscape complexity of forest disturbances. Statistics were calculated for all forest
173 disturbance patches larger than 1 ha and smaller than the 95th percentile of the patch size distribution
174 using the R package landscapemetrics [49]. We provide mean and standard deviation on edge, area,
175 their ratio and fractal dimension for both the historical and contemporary Hansen *et al.* [10] forest
176 cover maps.

177 We estimated above ground carbon (AGC) losses and gains over time using plot based averages
178 of recent inventory data at permanent sampling plots in the area (Figure 2). We refer to Kearsley *et al.*
179 [19] for the survey method and allometric relations used to scale the survey data. Unlike standard
180 square 1 ha plots edge plots were set back 200m from forest edges and were 50x200m, with the 50m
181 side of the plot along the forest edge and continuing 200m into the forest (Appendix Table 1). We
182 further confirmed that forest edge plots did not show a significantly different AGC compared to those
183 of non-edged / mixed forest plots (Mann Whitney U test, $p < 0.05$). Thus it was not necessary to
184 explicitly quantify changes in AGC caused by edge effects. Moreover, we used the mean values of the
185 mixed forest as representative for potential AGC losses. Despite the challenges inherent in quantifying
186 AGC for forest edges we mapped the total extent of the edges in the contemporary landscape. To
187 align our landscape analysis with exploratory analysis of the survey data we used a buffer of 200m to
188 estimate the extent of forest edges and patches, up to the location of forest edge plots.

189 Surveys of old plantations show a large variation in AGC, depending on age and the crop type.
190 For example, the AGC values varied from 168.67 to 86.55 g Mg C ha⁻¹, for *Hevea brasiliensis* (rubber
191 tree) and *Elaeis guineensis* (oil palm) plots respectively (Bustillo *et al.* [50], personal communications).
192 These higher values are in line with the mixed AGC estimates in the area, while the palm plantations
193 resemble old-regrowth values (81.8 Mg C ha⁻¹, see Table A1). We therefore use both the estimates
194 of old-regrowth and mixed forest to estimate AGC for regrowth. We did not have sufficient data to
195 account for individual changes in AGC across plantations.

196 **2.5. Canopy structure & FOTO texture analysis**

197 We compared the structure of the canopy both visually and using Fourier Transform Textural
198 Ordination (FOTO, Couteron [51]). Fourier Transform Textural Ordination uses a principal component

199 analysis (PCA) on radially averaged 2D Fourier spectra to characterize canopy (image) texture. The
200 FOTO technique was first described by Couteron [51] to quantify canopy stucture in relation to biomass
201 and biodiversity, and can be used across multiple scenes using normalization [35].

202 We used an area of 400x400m (16 ha) around contemporary permanent sampling plot locations to
203 quantify the general state of the canopy in both historical and contemporary pan-chromatic Geo-Eye 1
204 remote sensing data (GeoEye, 2012, Thornton, Colorado, U.S.A., order 737537, 2011-11-11 8:55h GMT or
205 9:55h local time). Geo-Eye data were resampled to the resolution of the historical data using a nearest
206 neighbour interpolation for comparison. For permanent sampling plot locations in both historical
207 and contemporary data a rectangular buffer of 200m around the centre of all plots was used to create
208 small image subsets. All image subsets were processed using the R based FOTO implementation
209 and package [52] using global normalization, ensuring intercomparability of texture metrics across
210 time and space [35]. We used a FOTO (moving) window size of 187 pixels (or ~150m), as described
211 in Solórzano *et al.* [53] and Barbier *et al.* [35], to ensure that multiple individual canopies could be
212 included in the analysis. A buffer with a radius of 50m around the center of all permanent sampling
213 plots was used to determine the average value of the first principle component (PC), explaining the
214 majority of the variance in canopy texture. Where both the Geo-Eye data and the orthomosaic image
215 overlapped we processed the intersecting region to explore a wall-to-wall comparison between past
216 and current canopy texture metrics.

217 We used the standard FOTO methodology with fixed zones, instead of the moving window
218 approach. The window size was set to the same size (187 pixels or ~150m) as used in the moving
219 window analysis above. To account for illumination differences between the two scenes we applied
220 histogram matching. No global normalization was applied, as the scene was processed as a whole. PC
221 values from this analysis for all permanent sampling plots in both image scences were extracted using
222 a buffer with a radius of 50m.

223 For both site based and scene analysis we correlate PC values with permanent sample plot
224 inventory data such as stem density, above ground biomass and tree species richness. Additional
225 comparisons are made between contemporary Geo-Eye data and the historical orthomosaic derived PC
226 values. Due to the few available permanent sampling plots in both scenes we used a non-parametric
227 paired signed rank (Wilcoxon) test to determine differences between the PC values of the Geo-Eye and
228 historical orthomosaic image scenes across mono-dominant and mixed forest types. In all analysis,
229 mono-dominant site 4 was removed from the analysis due to cloud contamination.

230 3. Results

231 Our analysis provides a first spatially explicit historical composite of aerial survey images
232 mapping LULCC within the Congo Basin. The use of high resolution historical images combined with
233 structure from motion image processing techniques allowed us to mosaic old imagery across a large
234 extent. The final orthomosaic composition of the Yangambi region resulted in an image scene covering
235 approximately 733 million pixels across ~828 km² (~23x36 km, Figure 2). The overall accuracy of the
236 structure from motion orthomosaic composition was 0.88 m/pixel using the sparse cloud DEM for
237 corrections at 45.8 m/pixel. The resulting georeferenced scene had a spatial accuracy of approximately
238 23m. Further georeferencing outside the SfM workflow reduced the mean error at the ground control
239 points to 5.3 ± 4.9 px (~ 4.7 ± 4.3 m), with a median error of 2.9 px (2.6m). The orthomosaic served
240 as input for all subsequent LULCC analysis with all derived maps provided with the manuscript
241 repository (see data & code availability statements below).

242 3.1. Land-use and Land-Cover Change & Above Ground Carbon

243 Our CNN deep learning classifier reached an Intersection-over-Union (IoU) accuracy of 97% on the
244 detection of disturbed forest in out-of-sample test data. A visual comparison on recent pan-chromatic
245 Geo-Eye 1 data shows good agreement, for a total of 87% of all pixels, between the landsat based
246 GFC data and downscaled CNN results (Appendix Table 3 and Figure 7). Scaling our classifier to the
247 whole historical orthomosaic we detected 162 km² (or ~20% of the scene) of disturbed forests. A large
248 fraction of the disturbed area was restored in the period between the two acquisitions. In total, 99 km²,
249 or little over half of the affected forest was restored (Figure 5C-D, dark blue). Recent deforested areas,
250 as registered through satellite remote sensing, approximate 88 km² (Table 1, Figure 5C-D / light green).

251 Recent deforestation follows a distinctly different pattern compared to historical patterns.
252 Historical deforestation showed a classical fishbone pattern for forest clearing with very sharp
253 edges, while current patterns are patchy and ad-hoc (figure 5D, dark blue and green colours
254 respectively). These differences are reflected in the analysis of landscape metrics of forest loss.
255 Between the historical and contemporary LULCC maps we see an increase in small disturbances,
256 as indicated by the decreasing area of the mean patch size, down to $\sim 1.86 \pm 0.75$ ha from $\sim 5.25 \pm$
257 5.02 ha historically. Perimeter lengths were longer historically, at 1451.58 ± 943.27 m, compared to
258 contemporary landscapes $\sim 921.74 \pm 362.59$ m (Table 2). This shift in perimeter area ratio led to a
259 similar change in the fractal index, increasing in value to 1.1 ± 0.05 from 1.09 ± 0.04 over time. Values
260 closer to a fractal index of 2 suggest a more complex (fragmented) landscape.

261 A comparison of forest edge plots with mixed forest plots showed no significant difference in
262 AGC, or other reported values such as species richness, basal area or stem density (Mann Whitney U

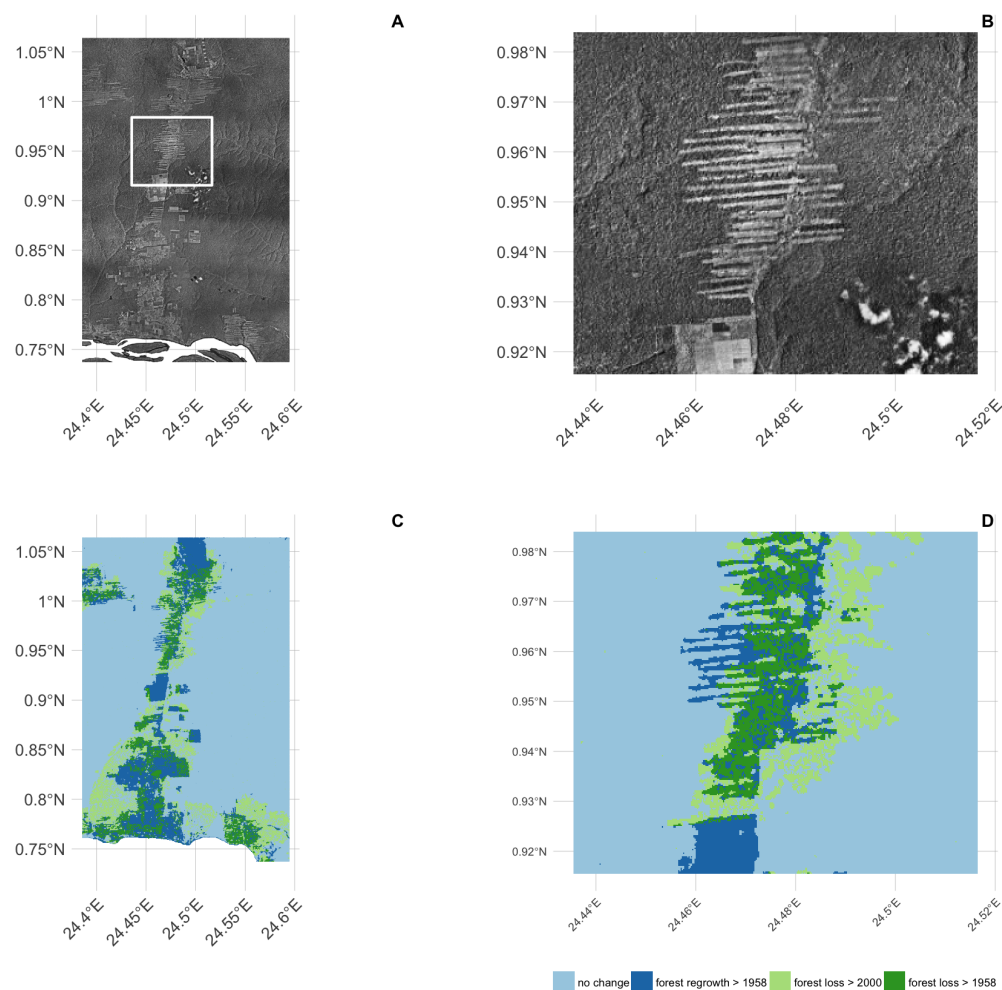


Figure 5. Overview of the final orthomosaic of the greater Yangambi region (A), a detailed inset (B) and the derived land use/land cover change map displayed as the difference between a manual classification of the orthomosaic and a recent map by Hansen et al. 2013 (C) and the corresponding land cover map for inset B (D).

²⁶³ test, $p < 0.05$). Edge influence did not extend beyond 200 m from a forest edge, but still represented an
²⁶⁴ area of 132 km².

²⁶⁵ Changes in both land-use and land-cover led to concomitant changes in above ground carbon
²⁶⁶ stocks. Recovery throughout the region was characterized for patches of forest and plantations.
²⁶⁷ Assuming high density stands, based on previous work, this could amount to a carbon gains of 1592
²⁶⁸ Gg C across our study area, offsetting more recent losses of approximately 1408 Gg C. On the other
²⁶⁹ hand, at the low end, if we assume a lower carbon density of 81.8 Mg C ha⁻¹ this would result in a
²⁷⁰ total carbon gain of 811 Gg C. Using our approach results indicate that overall deforestation around
²⁷¹ Yangambi has resulted in a loss of ~2416 Gg C in AGC stocks.

Table 1. Land use land cover change statistics of forest cover around Yangambi in the central Congo Basin. The data evaluates a difference between a historical (1958) aerial photography based survey and the Hansen et al. 2013 based satellite remote sensing data. Spatial coverage statistics are provided in square kilometers (km) and hectares (ha), rounded to the nearest integer as well as Above Ground Carbon (AGC) scaled using recent survey measurements.

	AGC		
	km ²	ha	(Gg C ha ⁻¹)
Forest	685	68455	-
- of which edges	132	13151	-
Regrowth > 1958 loss	99	9918	811 - 1592
Loss > 2000	88	8776	1408
Loss > 1958 (permanent)	63	6282	1008

Table 2. Landscape metrics for historical and contemporary deforestation patterns. We report patch perimeter and area, their ratio and fractal dimension. Values are reported as mean \pm standard deviation, across all deforestation patches.

	perimeter (m)	area (ha)	ratio (m^{-1})	fractal dimension
historical	1451.58 ± 943.27	5.25 ± 5.02	0.03 ± 0.01	1.09 ± 0.04
contemporary	921.74 ± 362.59	1.86 ± 0.75	0.05 ± 0.01	1.1 ± 0.05

²⁷² 3.2. Canopy structure & FOTO texture analysis

²⁷³ Visual interpretation of the scenes provide evidence that most locations do not change dramatically
²⁷⁴ with respect to canopy composition, except for the large areas of disturbances in contemporary fallow
²⁷⁵ or young-regrowth plots. One marked difference is noted in the mono-dominant site 6 (Appendix
²⁷⁶ Table 1). Here, the current mono-dominant *Brachystegia laurentii* is a recent development, changing the
²⁷⁷ canopy structure visibly during the last half century (Figure 6). The previous varied canopy structure
²⁷⁸ gave way to a more dense and uniform canopy. This is reflected in a change of the FOTO PC value from
²⁷⁹ 0.19 historically to its current value of 0.54. This historical value is similar to the mean of contemporary
²⁸⁰ mono-dominant stands with PC averaging 0.34 ± 0.1 , and is only slightly higher than historical values
²⁸¹ for a mixed forest (0.18 ± 0.08). The reverse pattern is seen in the contemporary PC values. Here, the

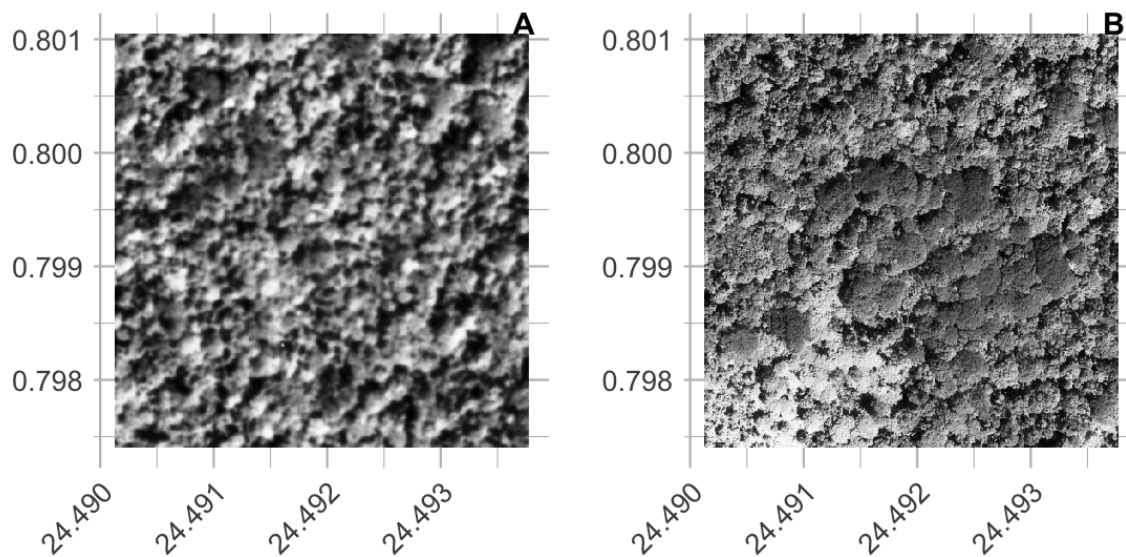


Figure 6. Visual comparison between a historical (A) and contemporary (B) permanent sampling plot. The site is currently listed as a mono-dominant *Brachystegia laurentii* stand. Note the structural differences with a 'coarse' canopy structure in the historical image compared to the more closed contemporary stand.

value of 0.54 exceeds those of most mono-dominant stands (0.35 ± 0.08), and is even further removed from the values noted for mixed forests (0.12 ± 0.03).

Using only small subsets around existing permanent sampling plots we show distinct differences between forest types, with PC values in both historical and contemporary imagery markedly higher for the mono-dominant forest types compared to all others (Appendix Figure 3). Provided that the young-regrowth and fallow permanent sampling plots have seen recent disturbance the Wilcoxon signed rank test on the mixed and mono-dominant plots between the historical and contemporary PC values did not show a significant difference ($p > 0.05$). Similarly, no significant difference using PC values extracted from the whole scene analysis was noted ($p > 0.05$). Any relationships between contemporary Geo-Eye data and permanent sampling plot measurements of Above Ground Biomass, stem density and species richness were non-significant ($p > 0.05$, Appendix Figures 4-6).

Furthermore, visual inspection of the scene wide analysis suggests historical scenes do not show landscape wide canopy features (Figure 7 A-B), unlike the contemporary scene (Figure 7 C-D). Where the FOTO algorithm picks up landscape features such as changes in texture across the contemporary Geo-Eye scene (e.g. the river valley as a diagonal line in Figure 7D), however, no corresponding landscape patterns are found by the FOTO algorithm in the historical orthomosaic.

4. Discussion

Finely grained spatial data sources, such as remote sensing imagery, are rare before the satellite era (<1970). This lack of data limits our understanding of how forest structure has varied over longer time

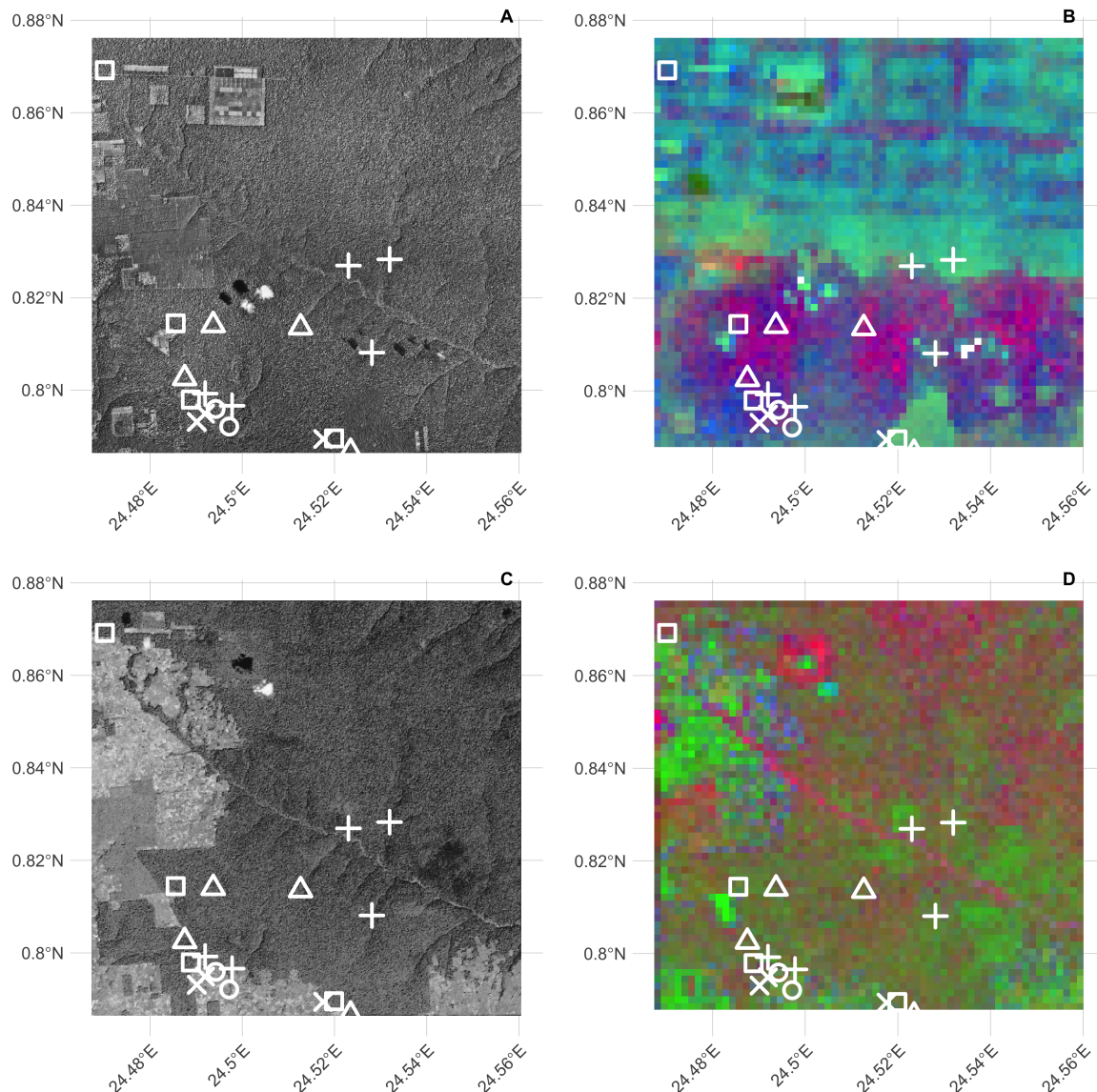


Figure 7. RGB visualizations of the first three principal components of scene wide FOTO texture analysis of historical and current (Geo-Eye) imagery. Current permanent sampling plots of mono-dominant, mixed, fallow and young (edge) forest plots are marked with open triangles, open circles, open squares and crosses, respectively.

301 periods in especially remote areas. Long term assessment can be extended by using large inventories
302 of historical aerial survey data [27,28,54]. However, across the Congo Basin this data is rare, or difficult
303 to access. Despite the difficulties in assessing hidden disturbances caused by deforestation, poorly
304 recorded official assessments or simply those invisible to standard remote sensing techniques [6],
305 remote sensing generally remains the best way to map and quantify LULCC [11]. Despite these
306 challenges in recovery and validation we present a first analysis of LULCC using historical aerial
307 survey data for the central Congo Basin. We used a combination of Structure-from-Motion and a
308 convolutional neural net deep learning approach to map deforestation across a large extent, providing
309 a long term view of LULCC in the central Congo Basin

310 *4.1. Data recovery challenges*

311 In our study the archive data recovered was limited to contact prints and therefore did not
312 represent the true resolution of the original negative. In addition, analogue photography clearly
313 produces a distinct softness compared to digital imagery (Figure 4). Despite favourable nadir image
314 acquisitions [55] image softness combined with illumination effects between flight paths, and the
315 self-similar nature of vast canopy expanses [56–58], limited our ability to provide wall-to-wall
316 coverage of the entire dataset containing 334 images. Few man made features in the scenes also
317 made georeferencing challenging. Although the village of Yangambi provided a range of buildings
318 as (hard-edge) references, other areas within the central Congo Basin might have fewer permanent
319 structures and would require the use of soft-edged landscape features (e.g. trees, river outflows).
320 Research has shown that soft-edged features can help georeference scenes even when containing
321 few man-made features [59], however accuracy becomes compromised. Our two step georeferencing
322 approach resulted in a referencing accuracy of $\sim 4.7 \pm 4.3$ m across reference points. However, it should
323 be noted that referencing accuracy of the final scene is less constrained toward the edges of the scene.

324 *4.2. Land-use, Land-Cover change & Above Ground Carbon*

325 When classifying our orthomosaic into forest and non-forest states we favoured a deep learning
326 supervised classification using a Convolutional Neural Network over manual segmentation to
327 guarantee an “apples-to-apples” comparison between the historical and the contemporary GFC forest
328 cover maps. We acknowledge that both classifications use different features, i.e. spectral or spatial data,
329 but attain a similarly high accuracy of 97% and 99% [10], for the GFC and our CNN map respectively.
330 Despite a number of challenges we were able to map and quantify a vast continuous area of tropical
331 forest, with limited manual annotation requirements.

332 Our analysis shows that the majority of deforestation around Yangambi happened toward the late
333 1950’s (162 km^2). Considerable regrowth has occurred since the aerial survey was executed (99 km^2),

and socio-economic instability prevented further large scale forest exploitation. In particular, many plantations have reached maturity and forest has re-established in previously cleared or disturbed areas. The majority of this forest recovery takes the form of isolated patches of forest but is offset by further deforestation of previously untouched forest. Generally, the function and structure of forests can be influenced by forest edges that are located up to 1km away however most effects are pronounced within the first 300m from the edge [60]. Our analysis of edge effects on AGC has shown that the influence is negligible 200m away from the edge. Phillips *et al.* [61] have shown similar weak responses to edge effects in the Amazon forest. Due to a lack of data on the extent (depth) of edge effects and their influence on AGC beyond 200m we did not include any estimates of carbon loss or gain within these zones. However, it must be stated that the influence of edges throughout the landscape was not marginal. as these areas would account for 132 km². Thus edges could have a substantial negative [9] or positive [62] influence on AGC. Similarly, uncertainties in how to explicitly correct for plantations in the landscape present a further challenge. Thus although our estimates are only indicative they do underscore the important influence of landscape structure when carbon accounting. However, our findings do not indicate that deforestation in Congo basin is declining, on the contrary.

Over the past half century there has been a clear shift in land use in Yangambi (Figure 5). Land use has shifted away from for example a regular fishbone deforestation pattern that emerges when (large scale) agricultural interests dominate the landscape [63], to a more fragmented landscape (Figure 5D). The latter former? is consistent with historical land management at the time of the aerial survey [50]. These regular patterns have since been reversed because of a decrease in large scale intensive agriculture, replaced by ad-hoc small scale subsistence farming with large perimeter to area relationships (i.e. ragged edges). Consequently, edge effects in the current landscape are far more pronounced than in the historical scene.

Visual inspection of the images also suggests that reforestation within the historically cleared areas and experimental plots is not necessarily limited to areas far removed from more densely populated areas. For example, large reforested areas exist close to the Congo stream and Yangambi village itself (Fig. 5). Here, regional political components, such as land leases and large scale ownership could have played a role in safeguarding some of these areas for rewilling or sustainable management [64,65]. Despite widespread anthropogenic influences throughout the tropics [37] the retention of these forested areas show the potential of explicit or implicit protective policy measures (e.g. INERA concessions, Bustillo *et al.* [50]) on a multi-decadal time scale. Forest regrowth in non-continuous areas within Yangambi could increase landscape connectivity and help increase biodiversity [15].

367 Our analysis therefore provides an opportunity to highlight and study those regions that have
368 previously suffered confirmed long-term disturbances, and those that have been restored since.
369 Assessments of old plantations and recovering clear-cut forests can serve as a guide to help estimate
370 carbon storage capacity and forest recovery rates in managed and unmanaged conditions [23,25,66]
371 over the mid- to long-term, in support of rewilding and general forest restoration [15,64,65]. In addition,
372 mapping long-term edge effects can further support research into issues such as receding forest edges
373 [60].

374 *4.3. Canopy structure & FOTO texture analysis*

375 Finally the FOTO technique used to quantify relationships between canopy structure and forest
376 characteristics rendered no valuable insights of either the historical orthomosaic or recent Geo-Eye
377 scene. Similarly weak correlations were found previously by Solórzano *et al.* [53]. In contrast site
378 based texture metric statistics did show correspondence between historical and contemporary satellite
379 imagery. However, none of them were either consistent or significant. Although visual interpretation
380 shows distinctly different canopy structures (Figure 5) the differences in how resolution is defined
381 and issues related to image quality prevented us from quantifying these further. Unlike large scale
382 studies by Ploton *et al.* [33] we could not scale this technique to historical data. We advise that future
383 valorisation efforts should preferentially work from foto negatives (if available) to ensure optimal data
384 quality in resolution, contrast and overall sharpness.

385 **5. Conclusion**

386 Given the impact of tropical forest disturbances on atmospheric CO₂ emissions, biodiversity and
387 ecosystem productivity accurate long term reporting on land-cover and land-use change especially
388 in the pre-satellite era is an imperative. Our analysis of historical aerial survey images of the Central
389 Congo Basin provides a window into the state of the forest at the start of the anthropocene. Efforts to
390 quantify canopy texture and their link to carbon storage had limited to no success. We have shown that
391 historical aerial survey data can be used to quantify land-use and land-cover change using a highly
392 automated workflow to quantify the structure and extent of forest cover change that can help assess
393 the impact of fragmentation on above ground carbon stocks. We also show a shift from previously
394 highly structured industrial deforestation of large areas, to discrete smallholder clearing for farming,
395 increasing landscape fragmentation but also opportunity for substantial regrowth. Efforts to quantify
396 canopy texture and their link to carbon storage had limited to no success. As such, our analysis
397 provides insights into the state of rarely studied tropical forests and the rate at which deforestation
398 and reforestation has taken place over a multi-decadal scale in the central Congo basin providing a

399 useful historical context to land-cover and land-use change spatial patterns for interpreting past and
400 ongoing field research in the area.

401 6. Additional Information and Declarations

402 6.1. Data availability

403 Hufkens et al. (2019). A curated dataset of aerial survey images over the central Congo Basin,
404 1958. Zenodo: doi.org/10.5281/zenodo.3547767. All data not included in the latter repository can be
405 found bundled with the analysis code as listed below. Proprietary datasets (i.e. Geo-Eye data) are not
406 shared, but purchase order numbers allow for acquisition of these datasets to ensure reproducibility.
407 The Hansen *et al.* [10] image data is freely available from [the GFC project website](#).

408 6.2. Code availability

409 All analysis code is available as an R / python [67] projects (<https://khufkens.github.io/orthodrc>
410 & https://khufkens.github.io/orthodrc_cnn/). The analysis relied heavily on the ‘raster’ [68],
411 ‘RStoolbox’ [69], and ‘landscapemetrics’ [49] packages, while post-processing and plotting was
412 facilitated by the ‘tidyverse’ ecosystem [70], ‘ggthemes’ [71], ‘scales’ [72] and ‘cowplot’ [73]. Additional
413 plotting elements were formatted or provided by ‘sf’ [74] and ‘rnaturalearth’ [75] packages, respectively.
414 I’m grateful for the contributions to the scientific community by the developers of these packages.

415 **Acknowledgments:** This research was supported through the Belgian Science Policy office COBECORE
416 project (BELSPO; grant BR/175/A3/COBECORE). KH acknowledges funding from the European Union Marie
417 Skłodowska-Curie Action (project number 797668). I’m grateful for the support of Thales D’Haulleville
418 volunteering his time in scanning the images.

419 **Author Contributions:** K.H. conceived and designed the study, analyzed the data, prepared figures and tables,
420 authored, reviewed and approved the final draft of the manuscript. T.d.H. scanned all image data. E.K. and T.d.H.
421 provided plot based AGC estimates. T.D., K.J., E.K, H.B., P.S., F.V,S.M., M.A., J.V.D.B., H.V and L.W. reviewed the
422 final manuscript.

423 **Conflicts of Interest:** The authors declare no conflict of interest. The founding sponsors had no role in the design
424 of the study; in the collection, analyses, or interpretation of data; in the writing of the manuscript, an in the
425 decision to publish the results.

426 References

- 427 1. Butsic, V.; Baumann, M.; Shortland, A.; Walker, S.; Kuemmerle, T. Conservation and conflict in the
428 Democratic Republic of Congo: The impacts of warfare, mining, and protected areas on deforestation.
429 *Biological Conservation* **2015**, *191*, 266–273. doi:10.1016/j.biocon.2015.06.037.
- 430 2. Laurance, W.F.; Delamônica, P.; Laurance, S.G.; Vasconcelos, H.L.; Lovejoy, T.E. Rainforest fragmentation
431 kills big trees. *Nature* **2000**, *404*, 836–836. doi:10.1038/35009032.
- 432 3. Magnago, L.F.S.; Magrach, A.; Laurance, W.F.; Martins, S.V.; Meira-Neto, J.A.A.; Simonelli, M.; Edwards,
433 D.P. Would protecting tropical forest fragments provide carbon and biodiversity cobenefits under REDD+?
434 *Global Change Biology* **2015**, *21*, 3455–3468. doi:10.1111/gcb.12937.

- 435 4. Poorter, L.; Bongers, F. Leaf traits are good predictors of plant performance across 53 rain forest species.
436 *Ecology* **2006**, *87*, 1733–1743. doi:10.1890/0012-9658(2006)87[1733:LTAGPO]2.0.CO;2.
- 437 5. Didham, R.K. Edge Structure Determines the Magnitude of Changes in Microclimate and Vegetation
438 Structure in Tropical Forest Fragments. *Biotropica* **1999**, *31*, 17–30.
- 439 6. Peres, C.A.; Barlow, J.; Laurance, W.F. Detecting anthropogenic disturbance in tropical forests. *Trends in*
440 *Ecology & Evolution* **2006**, *21*, 227–229. doi:10.1016/j.tree.2006.03.007.
- 441 7. Stark, S.C.; Leitold, V.; Wu, J.L.; Hunter, M.O.; de Castilho, C.V.; Costa, F.R.C.; McMahon, S.M.; Parker,
442 G.G.; Shimabukuro, M.T.; Lefsky, M.A.; Keller, M.; Alves, L.F.; Schietti, J.; Shimabukuro, Y.E.; Brandão,
443 D.O.; Woodcock, T.K.; Higuchi, N.; de Camargo, P.B.; de Oliveira, R.C.; Saleska, S.R. Amazon forest
444 carbon dynamics predicted by profiles of canopy leaf area and light environment. *Ecology Letters* **2012**,
445 *15*, 1406–1414. doi:10.1111/j.1461-0248.2012.01864.x.
- 446 8. Fauset, S.; Gloor, M.U.; Aidar, M.P.M.; Freitas, H.C.; Fyllas, N.M.; Marabesi, M.A.; Rochelle, A.L.C.;
447 Shenkin, A.; Vieira, S.A.; Joly, C.A. Tropical forest light regimes in a human-modified landscape. *Ecosphere*
448 **2017**, *8*, e02002. doi:10.1002/ecs2.2002.
- 449 9. Brinck, K.; Fischer, R.; Groeneveld, J.; Lehmann, S.; Dantas De Paula, M.; Pütz, S.; Sexton, J.O.; Song, D.;
450 Huth, A. High resolution analysis of tropical forest fragmentation and its impact on the global carbon
451 cycle. *Nature Communications* **2017**, *8*. doi:10.1038/ncomms14855.
- 452 10. Hansen, M.C.; Potapov, P.V.; Moore, R.; Hancher, M.; Turubanova, S.A.; Tyukavina, A.; Thau, D.; Stehman,
453 S.V.; Goetz, S.J.; Loveland, T.R.; Kommareddy, A.; Egorov, A.; Chini, L.; Justice, C.O.; Townshend,
454 J.R.G. High-Resolution Global Maps of 21st-Century Forest Cover Change. *Science* **2013**, *342*, 850–853.
455 doi:10.1126/science.1244693.
- 456 11. Houghton, R.A.; House, J.I.; Pongratz, J.; van der Werf, G.R.; DeFries, R.S.; Hansen, M.C.; Le Quéré, C.;
457 Ramankutty, N. Carbon emissions from land use and land-cover change. *Biogeosciences* **2012**, *9*, 5125–5142.
458 doi:10.5194/bg-9-5125-2012.
- 459 12. Tyukavina, A.; Baccini, A.; Hansen, M.C.; Potapov, P.V.; Stehman, S.V.; Houghton, R.A.; Krylov, A.M.;
460 Turubanova, S.; Goetz, S.J. Aboveground carbon loss in natural and managed tropical forests from 2000 to
461 2012. *Environmental Research Letters* **2015**, *10*, 074002. doi:10.1088/1748-9326/10/7/074002.
- 462 13. van der Werf, G.R.; Morton, D.C.; DeFries, R.S.; Olivier, J.G.J.; Kasibhatla, P.S.; Jackson, R.B.; Collatz, G.J.;
463 Randerson, J.T. CO₂ emissions from forest loss. *Nature Geoscience* **2009**, *2*, 737–738. doi:10.1038/ngeo671.
- 464 14. Barlow, J.; Lennox, G.D.; Ferreira, J.; Berenguer, E.; Lees, A.C.; Nally, R.M.; Thomson, J.R.; Ferraz, S.F.d.B.;
465 Louzada, J.; Oliveira, V.H.F.; Parry, L.; Ribeiro de Castro Solar, R.; Vieira, I.C.G.; Aragão, L.E.O.C.; Begotti,
466 R.A.; Braga, R.F.; Cardoso, T.M.; Jr, R.C.d.O.; Souza Jr, C.M.; Moura, N.G.; Nunes, S.S.; Siqueira, J.V.;
467 Pardini, R.; Silveira, J.M.; Vaz-de Mello, F.Z.; Veiga, R.C.S.; Venturieri, A.; Gardner, T.A. Anthropogenic
468 disturbance in tropical forests can double biodiversity loss from deforestation. *Nature* **2016**, *535*, 144–147.
469 doi:10.1038/nature18326.
- 470 15. Van de Perre, F.; Willig, M.R.; Presley, S.J.; Bapeamoni Andemwana, F.; Beeckman, H.; Boeckx, P.; Cooleman,
471 S.; de Haan, M.; De Kesel, A.; Dessein, S.; Grootaert, P.; Huygens, D.; Janssens, S.B.; Kearsley, E.; Kabeya,
472 P.M.; Leponce, M.; Van den Broeck, D.; Verbeeck, H.; Würsten, B.; Leirs, H.; Verheyen, E. Reconciling
473 biodiversity and carbon stock conservation in an Afrotropical forest landscape. *Science Advances* **2018**,
474 *4*, eaar6603. doi:10.1126/sciadv.aar6603.
- 475 16. Lewis, S.L.; Lopez-Gonzalez, G.; Sonké, B.; Affum-Baffoe, K.; Baker, T.R.; Ojo, L.O.; Phillips, O.L.; Reitsma,
476 J.M.; White, L.; Comiskey, J.A.; Djuikouo K, M.N.; Ewango, C.E.N.; Feldpausch, T.R.; Hamilton, A.C.;
477 Gloor, M.; Hart, T.; Hladik, A.; Lloyd, J.; Lovett, J.C.; Makana, J.R.; Malhi, Y.; Mbago, F.M.; Ndangalasi,
478 H.J.; Peacock, J.; Peh, K.S.H.; Sheil, D.; Sunderland, T.; Swaine, M.D.; Taplin, J.; Taylor, D.; Thomas, S.C.;
479 Votere, R.; Wöll, H. Increasing carbon storage in intact African tropical forests. *Nature* **2009**, *457*, 1003–1006.
480 Publisher: Earth and Biosphere Institute, School of Geography, University of Leeds, Leeds LS2 9JT, UK.
481 s.l.lewis@leeds.ac.uk.
- 482 17. Verbeeck, H.; Boeckx, P.; Steppe, K. Tropical forests: include Congo basin. *Nature* **2011**, *479*, 179–179.
- 483 18. Lewis, S.L.; Sonke, B.; Sunderland, T.; Begne, S.K.; Lopez-Gonzalez, G.; van der Heijden, G.M.F.; Phillips,
484 O.L.; Affum-Baffoe, K.; Baker, T.R.; Banin, L.; Bastin, J.F.; Beeckman, H.; Boeckx, P.; Bogaert, J.; De Canniere,
485 C.; Chezeaux, E.; Clark, C.J.; Collins, M.; Djagbletey, G.; Djuikouo, M.N.K.; Droissart, V.; Doucet, J.L.;
486 Ewango, C.E.N.; Fauset, S.; Feldpausch, T.R.; Foli, E.G.; Gillet, J.F.; Hamilton, A.C.; Harris, D.J.; Hart, T.B.;
487 de Haulleville, T.; Hladik, A.; Hufkens, K.; Huygens, D.; Jeanmart, P.; Jeffery, K.J.; Kearsley, E.; Leal, M.E.;

- 488 Lloyd, J.; Lovett, J.C.; Makana, J.R.; Malhi, Y.; Marshall, A.R.; Ojo, L.; Peh, K.S.H.; Pickavance, G.; Poulsen,
489 J.R.; Reitsma, J.M.; Sheil, D.; Simo, M.; Steppe, K.; Taedoumg, H.E.; Talbot, J.; Taplin, J.R.D.; Taylor, D.;
490 Thomas, S.C.; Toirambe, B.; Verbeeck, H.; Vleminckx, J.; White, L.J.T.; Willcock, S.; Woell, H.; Zemagho, L.
491 Above-ground biomass and structure of 260 African tropical forests. *Philosophical Transactions of the Royal
492 Society B: Biological Sciences* **2013**, *368*, 20120295–20120295. doi:10.1098/rstb.2012.0295.
- 493 19. Kearsley, E.; de Haulleville, T.; Hufkens, K.; Kidimbu, A.; Toirambe, B.; Baert, G.; Huygens, D.; Kebede,
494 Y.; Defourny, P.; Bogaert, J.; Beeckman, H.; Steppe, K.; Boeckx, P.; Verbeeck, H. Conventional tree
495 height-diameter relationships significantly overestimate aboveground carbon stocks in the Central Congo
496 Basin. *Nature communications* **2013**, *4*, 2269. doi:10.1038/ncomms3269.
- 497 20. Doetterl, S.; Kearsley, E.; Bauters, M.; Hufkens, K.; Lisingo, J.; Baert, G.; Verbeeck, H.; Boeckx, P.
498 Aboveground vs. Belowground Carbon Stocks in African Tropical Lowland Rainforest: Drivers and
499 Implications. *Plos One* **2015**, *10*, e0143209. doi:10.1371/journal.pone.0143209.
- 500 21. Ramankutty, N.; Foley, J.A. Estimating historical changes in global land cover: Croplands from 1700 to
501 1992. *Global Biogeochemical Cycles* **1999**, *13*, 997–1027. doi:10.1029/1999GB900046.
- 502 22. DeFries, R.S.; Houghton, R.A.; Hansen, M.C.; Field, C.B.; Skole, D.; Townshend, J. Carbon emissions from
503 tropical deforestation and regrowth based on satellite observations for the 1980s and 1990s. *Proceedings of
504 the National Academy of Sciences* **2002**, *99*, 14256–14261. doi:10.1073/pnas.182560099.
- 505 23. Sader, S.A.; Joyce, A.T. Deforestation Rates and Trends in Costa Rica, 1940 to 1983. *Biotropica* **1988**, *20*, 11.
506 doi:10.2307/2388421.
- 507 24. Houghton, R. How well do we know the flux of CO₂ from land-use change? *Tellus B: Chemical and Physical
508 Meteorology* **2010**, *62*, 337–351. doi:10.1111/j.1600-0889.2010.00473.x.
- 509 25. Achard, F.; Beuchle, R.; Mayaux, P.; Stibig, H.J.; Bodart, C.; Brink, A.; Carboni, S.; Desclée, B.; Donnay, F.;
510 Eva, H.D.; Lupi, A.; Raši, R.; Seliger, R.; Simonetti, D. Determination of tropical deforestation rates and
511 related carbon losses from 1990 to 2010. *Global Change Biology* **2014**, *20*, 2540–2554. doi:10.1111/gcb.12605.
- 512 26. Mitchard, E.T.A. The tropical forest carbon cycle and climate change. *Nature* **2018**, *559*, 527–534.
513 doi:10.1038/s41586-018-0300-2.
- 514 27. Song, D.X.; Huang, C.; Sexton, J.O.; Channan, S.; Feng, M.; Townshend, J.R. Use of Landsat and
515 Corona data for mapping forest cover change from the mid-1960s to 2000s: Case studies from the Eastern
516 United States and Central Brazil. *ISPRS Journal of Photogrammetry and Remote Sensing* **2015**, *103*, 81–92.
517 doi:10.1016/j.isprsjprs.2014.09.005.
- 518 28. Nita, M.D.; Munteanu, C.; Gutman, G.; Abrudan, I.V.; Radloff, V.C. Widespread forest cutting in the
519 aftermath of World War II captured by broad-scale historical Corona spy satellite photography. *Remote
520 Sensing of Environment* **2018**, *204*, 322–332. doi:10.1016/j.rse.2017.10.021.
- 521 29. Giordano, S.; Le Bris, A.; Mallet, C. Toward automatic georeferencing of archival aerial photogrammetric
522 surveys. *ISPRS Annals of Photogrammetry, Remote Sensing and Spatial Information Sciences* **2018**, IV-2, 105–112.
523 doi:10.5194/isprs-annals-IV-2-105-2018.
- 524 30. Buitenwerf, R.; Bond, W.J.; Stevens, N.; Trollope, W.S.W. Increased tree densities in South African
525 savannas: >50 years of data suggests CO₂ as a driver. *Global Change Biology* **2012**, *18*, 675–684.
526 doi:10.1111/j.1365-2486.2011.02561.x.
- 527 31. Okeke, F.; Karnieli, A. Methods for fuzzy classification and accuracy assessment of historical aerial
528 photographs for vegetation change analyses. Part I: Algorithm development. *International Journal of Remote
529 Sensing* **2006**, *27*, 153–176. doi:10.1080/01431160500166540.
- 530 32. Frankl, A.; Seghers, V.; Stal, C.; De Maeyer, P.; Petrie, G.; Nyssen, J. Using image-based modelling
531 (SfM-MVS) to produce a 1935 ortho-mosaic of the Ethiopian highlands. *International Journal of Digital Earth*
532 **2015**, *8*, 421–430. doi:10.1080/17538947.2014.942715.
- 533 33. Ploton, P.; Pélassier, R.; Proisy, C.; Flavenot, T.; Barbier, N.; Rai, S.N.; Couteron, P. Assessing aboveground
534 tropical forest biomass using Google Earth canopy images. *Ecological Applications* **2012**, *22*, 993–1003.
- 535 34. Couteron, P.; Pelissier, R.; Nicolini, E.a.; Paget, D. Predicting tropical forest stand structure parameters
536 from Fourier transform of very high-resolution remotely sensed canopy images. *Journal of Applied Ecology*
537 **2005**, *42*, 1121–1128. doi:10.1111/j.1365-2664.2005.01097.x.
- 538 35. Barbier, N.; Couteron, P.; Proisy, C.; Malhi, Y.; Gastellu-Etchegorry, J.P. The variation of apparent crown
539 size and canopy heterogeneity across lowland Amazonian forests. *Global Ecology and Biogeography* **2010**,
540 *19*, 72–84. doi:10.1111/j.1466-8238.2009.00493.x.

- 541 36. Willcock, S.; Phillips, O.L.; Platts, P.J.; Swetnam, R.D.; Balmford, A.; Burgess, N.D.; Ahrends, A.; Bayliss,
542 J.; Doggart, N.; Doody, K.; Fanning, E.; Green, J.M.H.; Hall, J.; Howell, K.L.; Lovett, J.C.; Marchant, R.;
543 Marshall, A.R.; Mbilinyi, B.; Munishi, P.K.T.; Owen, N.; Topp-Jorgensen, E.J.; Lewis, S.L. Land cover
544 change and carbon emissions over 100 years in an African biodiversity hotspot. *Global Change Biology* **2016**,
545 22, 2787–2800. doi:10.1111/gcb.13218.
- 546 37. Lewis, S.L.; Maslin, M.A. Defining the Anthropocene. *Nature* **2015**, 519, 171–180. doi:10.1038/nature14258.
- 547 38. Bauters, M.; Ampoorter, E.; Huygens, D.; Kearsley, E.; De Hauville, T.; Sellan, G.; Verbeeck, H.; Boeckx,
548 P.; Verheyen, K. Functional identity explains carbon sequestration in a 77-year-old experimental tropical
549 plantation. *Ecosphere* **2015**, 6, art198. doi:10.1890/ES15-00342.1.
- 550 39. Zuiderveld, K. Contrast Limited Adaptive Histogram Equalization. In *Graphics GEMs IV*; Academic Press:
551 San Diego, CA, USA, 1994; pp. 474–485.
- 552 40. Ullman, S. The Interpretation of Structure from Motion. *Proceedings of the Royal Society of London. Series B,
553 Biological Sciences* **1979**, 203, 405–426.
- 554 41. QGIS Development team,. QGIS Geographic Information System., 2018.
- 555 42. Ronneberger, O.; Fischer, P.; Brox, T. U-Net: Convolutional Networks for Biomedical Image Segmentation.
556 In *Medical Image Computing and Computer-Assisted Intervention – MICCAI 2015*; Navab, N.; Hornegger, J.;
557 Wells, W.M.; Frangi, A.F., Eds.; Springer International Publishing: Cham, 2015; Vol. 9351, pp. 234–241.
558 doi:10.1007/978-3-319-24574-4_28.
- 559 43. Chollet, F. *Keras*; GitHub, 2015.
- 560 44. Yakubovskiy, P. *Segmentation Models*; GitHub, 2019.
- 561 45. Martín Abadi.; Ashish Agarwal.; Paul Barham.; Eugene Brevdo.; Zhifeng Chen.; Craig Citro.; Greg S.
562 Corrado.; Andy Davis.; Jeffrey Dean.; Matthieu Devin.; Sanjay Ghemawat.; Ian Goodfellow.; Andrew
563 Harp.; Geoffrey Irving.; Michael Isard.; Jia, Y.; Rafal Jozefowicz.; Lukasz Kaiser.; Manjunath Kudlur.; Josh
564 Levenberg.; Dandelion Mané.; Rajat Monga.; Sherry Moore.; Derek Murray.; Chris Olah.; Mike Schuster.;
565 Jonathon Shlens.; Benoit Steiner.; Ilya Sutskever.; Kunal Talwar.; Paul Tucker.; Vincent Vanhoucke.; Vijay
566 Vasudevan.; Fernanda Viégas.; Oriol Vinyals.; Pete Warden.; Martin Wattenberg.; Martin Wicke.; Yuan Yu.;
567 Xiaoqiang Zheng. *TensorFlow: Large-Scale Machine Learning on Heterogeneous Systems*; 2015.
- 568 46. Buscombe, D.; Ritchie, A. Landscape Classification with Deep Neural Networks. *Geosciences* **2018**, 8, 244.
569 doi:10.3390/geosciences8070244.
- 570 47. Kingma, D.P.; Ba, J. Adam: A Method for Stochastic Optimization. *arXiv:1412.6980 [cs]* **2017**. arXiv:
571 1412.6980.
- 572 48. Dale, M.R.T. *Spatial pattern analysis in plant ecology*; Cambridge studies in ecology, Cambridge University
573 Press: Cambridge ; New York, 1999.
- 574 49. Hesselbarth, M.H.K.; Sciaiani, M.; With, K.A.; Wiegand, K.; Nowosad, J. landscapemetrics: an open-source
575 R tool to calculate landscape metrics. *Ecography* **2019**.
- 576 50. Bustillo, E.; Raets, L.; Beeckman, H.; Bourland, N.; Rousseau, M.; Hubau, W.; De Mil, T. Evaluation du
577 potentiel énergétique de la biomasse aérienne ligneuse des anciennes plantations de l'INERA Yangambi.
578 Technical report, CIFOR, 2018.
- 579 51. Couturon, P. Quantifying change in patterned semi-arid vegetation by Fourier analysis of digitized aerial
580 photographs. *International Journal of Remote Sensing* **2002**, 23, 3407–3425. doi:10.1080/01431160110107699.
- 581 52. Hufkens, K. foto: an R implementation of the "fourier transform textural ordination (foto)" method., 2019.
- 582 53. Solórzano, J.V.; Gallardo-cruz, J.A.; González, E.J.; Peralta-carreta, C.; Hernández-gómez, M.; Oca,
583 A.F.m.D.; Cervantes-jiménez, L.G.; Solórzano, J.V.; Gallardo-cruz, J.A.; González, E.J.; Peralta-carreta,
584 C.; Hernández-gómez, M.; Oca, A.F.m.D.; Cervantes-jiménez, L.G. Contrasting the potential of
585 Fourier transformed ordination and gray level co-occurrence matrix textures to model a tropical swamp
586 forest ' s structural and diversity attributes. *Journal of Applied Remote Sensing* **2018**, 12, 036006.
587 doi:10.1117/1.JRS.12.036006.
- 588 54. Kadmon, R.; Harari-Kremer, R. Studying Long-Term Vegetation Dynamics Using Digital
589 Processing of Historical Aerial Photographs. *Remote Sensing of Environment* **1999**, 68, 164–176.
590 doi:10.1016/S0034-4257(98)00109-6.
- 591 55. Verhoeven, G. BRDF and its Impact on Aerial Archaeological Photography: BRDF and its impact on aerial
592 archaeologal photography. *Archaeological Prospection* **2017**, 24, 133–140. doi:10.1002/arp.1559.

- 593 56. Park, J.Y.; Muller-Landau, H.C.; Lichstein, J.W.; Rifai, S.W.; Dandois, J.P.; Bohlman, S.A. Quantifying Leaf
594 Phenology of Individual Trees and Species in a Tropical Forest Using Unmanned Aerial Vehicle (UAV)
595 Images. *Remote Sensing* **2019**, *11*, 1534. doi:10.3390/rs11131534.
- 596 57. Simini, F.; Anfodillo, T.; Carrer, M.; Banavar, J.R.; Maritan, A. Self-similarity and scaling
597 in forest communities. *Proceedings of the National Academy of Sciences* **2010**, *107*, 7658–7662.
598 doi:10.1073/pnas.1000137107.
- 599 58. Sole, R.V.; Manrubia, S.C. Self-similarity in rain forests: evidence for a critical state. *Physical Review E* **1995**,
600 51, 6250 – 6253.
- 601 59. Hughes, M.L.; McDowell, P.F.; Marcus, W.A. Accuracy assessment of georectified aerial photographs:
602 Implications for measuring lateral channel movement in a GIS. *Geomorphology* **2006**, *74*, 1–16.
603 doi:10.1016/j.geomorph.2005.07.001.
- 604 60. Gascon, C.; Williamson, G.B.; Fonseca, G.A.B.d. Receding Forest Edges and Vanishing Reserves. *Science,*
605 *New Series* **2000**, *288*, 1356–1358.
- 606 61. Phillips, O.L.; Rose, S.; Mendoza, A.M.; Vargas, P.N. Resilience of Southwestern Amazon Forests to
607 Anthropogenic Edge Effects. *Conservation Biology* **2006**, *20*, 1698–1710. doi:10.1111/j.1523-1739.2006.00523.x.
- 608 62. Reinmann, A.B.; Hutyra, L.R. Edge effects enhance carbon uptake and its vulnerability to climate
609 change in temperate broadleaf forests. *Proceedings of the National Academy of Sciences* **2017**, *114*, 107–112.
610 doi:10.1073/pnas.1612369114.
- 611 63. Arima, E.Y.; Walker, R.T.; Perz, S.; Souza, C. Explaining the fragmentation in the Brazilian Amazonian
612 forest. *Journal of Land Use Science* **2015**, pp. 1–21. doi:10.1080/1747423X.2015.1027797.
- 613 64. Arima, E.Y.; Barreto, P.; Araújo, E.; Soares-Filho, B. Public policies can reduce tropical deforestation: Lessons
614 and challenges from Brazil. *Land Use Policy* **2014**, *41*, 465–473. doi:10.1016/j.landusepol.2014.06.026.
- 615 65. Larson, A.M. Forest tenure reform in the age of climate change: Lessons for REDD+. *Global Environmental
616 Change* **2011**, *21*, 540–549. doi:10.1016/j.gloenvcha.2010.11.008.
- 617 66. Gourlet-Fleury, S.; Mortier, F.; Fayolle, A.; Baya, F.; Ouédraogo, D.; Bénédet, F.; Picard, N. Tropical forest
618 recovery from logging: a 24 year silvicultural experiment from Central Africa. *Philosophical Transactions of
619 the Royal Society B: Biological Sciences* **2013**, *368*, 20120302. doi:10.1098/rstb.2012.0302.
- 620 67. R Core Team. *R: A Language and Environment for Statistical Computing*; R Foundation for Statistical
621 Computing: Vienna, Austria, 2019.
- 622 68. Hijmans, R.J. *raster: Geographic Data Analysis and Modeling*; 2019.
- 623 69. Leutner, B.; Horning, N.; Schwalb-Willmann, J. *RStoolbox: Tools for Remote Sensing Data Analysis*; 2019.
- 624 70. Wickham, H. *tidyverse: Easily Install and Load the 'Tidyverse'*; 2017.
- 625 71. Arnold, J.B. *ggthemes: Extra Themes, Scales and Geoms for 'ggplot2'*; 2019.
- 626 72. Wickham, H. *scales: Scale Functions for Visualization*; 2018.
- 627 73. Wilke, C.O. *cowplot: Streamlined Plot Theme and Plot Annotations for 'ggplot2'*; 2019.
- 628 74. Pebesma, E. Simple Features for R: Standardized Support for Spatial Vector Data. *The R Journal* **2018**,
629 *10*, 439–446. doi:10.32614/RJ-2018-009.
- 630 75. South, A. *rnatnuralearth: World Map Data from Natural Earth*; 2017.

631 © 2019 by the authors. Submitted to *Remote Sens.* for possible open access publication
632 under the terms and conditions of the Creative Commons Attribution (CC BY) license
633 (<http://creativecommons.org/licenses/by/4.0/>).